Improved Imaging of the Large-Scale Structure of a Groundwater System with Airborne Electromagnetic Data

Seogi Kang[1], Rosemary Knight[1], and Meredith Goebel[1]

[1]Stanford University

Corresponding author: Seogi Kang (sgkang09@stanford.edu)

Key Points:

- Airborne electromagnetic (AEM) data were used to map out the large-scale structure in the groundwater model of the Kaweah subbasin in California's Central Valley.
- A new approach to the inversion of AEM data improved the accuracy in estimates of the depth to bedrock and the depth and thickness of the confining Corcoran Clay layer.
- The defined large-scale structure was used in a structurally-constrained inversion of the AEM data to improve the imaging of smaller-scale structure.

Abstract

Working with airborne electromagnetic (AEM) data acquired in the Kaweah Subbasin in the Central Valley of California, U.S.A., we developed a new approach for imaging the top of the bedrock and the confining Corcoran Clay layer. Our approach included multiple L_2-norm and L_p-norm inversions as well as an interpolation process. The major improvement in imaging the two targets was made in the L_p-norm inversion step by incorporating prior knowledge. For the Corcoran Clay, pairs of resistivity and driller's logs at two wells guided the selection of the best resistivity model and were used to increase the accuracy of the estimated Clay thickness. The bedrock surface was poorly constrained by well data in the existing groundwater model, appearing as a flat surface. We had good AEM data coverage in the area so had higher confidence in the obtained map of the bedrock surface at depths ranging from 15 m to 160 m. There was relatively good agreement between the location of the Corcoran Clay in the AEM data (depth ranging from 50 to 130 m and thickness ranging from 3 to 25 m) and the existing groundwater model, with both depth and thickness showing ~15% relative difference. The AEM data provided information about the continuity of the Corcoran Clay that is challenging to capture in the well data. The locations of the bedrock and Corcoran Clay were used in a structurally-constrained inversion to improve the imaging of the smaller-scale resistivity structure.

1 Introduction

With climate change and population growth, there is increasing concern about the depletion of groundwater resources and recognition of the need for sustainable management. A groundwater model is the foundation on which to build effective groundwater science and management. Required to inform the development of the groundwater model is information about the subsurface that captures spatial heterogeneity at the level needed as the input for flow modeling. All groundwater models include some representation of the large-scale structure of the groundwater system – the hydrogeologic units and other major features relevant for modeling flow. Information derived from driller's logs, recorded when wells are drilled, is typically used to build the model. The logs potentially provide valuable information at point locations, but the quality of the driller's logs can be highly variable and challenging to quantify. In addition, the spatial density of the driller's logs might be too low to adequately capture the continuity of the large-scale subsurface features. Uncertainty in representing the large-scale structure can have a significant impact on the predictions obtained from a groundwater model.

The airborne electromagnetic (AEM) method is potentially a highly effective means of imaging large-scale structure for the development of a groundwater model (Foged et al., 2013; Kang et al., 2021; Knight et al., 2018; Sattel & Kgotlhang, 2004; Wynn, 2002). Inversion of the acquired AEM data recovers a resistivity model of the subsurface which can be transformed, through the use of well data, to a model displaying the variation in lithology or sediment type. This observed variation can then be interpreted to identify the large-scale features of the groundwater system, e.g. mapping out the lithologic units or sediment packages that define the major aquifers and aquitards. One challenge when using the AEM method for this application, however, is the limited spatial resolution of the method resulting in uncertainty in the recovered resistivity model and interpreted locations of the large-scale features.

In this study, we developed a new approach to the AEM inversion workflow. This approach was designed for the scenario where AEM data are being acquired in an area with no existing groundwater model and limited high-quality well data. Our objective was to achieve improved imaging of the subsurface so as to capture, as accurately as possible, the large-scale features required for developing a groundwater model using the AEM data and high-quality well data from a few locations. We accomplished this through a "targeted inversion approach" where we defined as targets specific features which we wanted to accurately resolve in our study area – the bedrock surface (at the top of the bedrock) underlying the sediments of the aquifer system and the confining clay layer dividing the system into an upper and lower aquifer. While these two features were defined for our study area, the Kaweah Subbasin located in California's Central Valley, U.S.A., they define part of the large-scale structure in many groundwater systems throughout the Central Valley and elsewhere in the world. Using the commonly-adopted L_2-norm approach to the inversion of AEM data, a bedrock surface will appear as a smooth transition rather than a distinct boundary in the recovered resistivity model, introducing uncertainty in its location. Similarly, the lack of a distinct boundary at the upper and lower boundaries of a clay layer will introduce uncertainty in its location and can cause the thickness of the layer to be significantly overestimated. Errors in the depth to bedrock and the thickness of the confining layer could significantly impact the accuracy of the results obtained from a groundwater model.

Our targeted inversion approach utilized a multi-step inversion process which included both the standard L_2-norm inversion and the L_p-norm inversion (Fournier & Oldenburg, 2019), the latter allowing us to incorporate prior knowledge about the targets. To form 2D maps displaying the locations of the targets – the large-scale features, we integrated high-quality well data and the resistivity models recovered through L_2-norm and L_p-norm inversions. To demonstrate the efficacy of our approach, the locations of the targets that we obtained were compared with the locations within the existing groundwater model which had been constructed using available well data. Once the large-scale structure had been identified, this was used in a final inversion to obtain improved imaging of the smaller-scale structure. Through the developed multi-step approach, we formalized a process, readily transferable to other locations, designed to obtain improved imaging of groundwater systems from AEM data.

2 Background

2.1 Hydrogeology and existing groundwater model in the study area

The Kaweah Subbasin is located in the southern part of the Central Valley, referred to as the San Joaquin Valley, with the eastern edge defined as the interface between the valley floor and the foothills of the Sierra Nevada Mountains. As part of their efforts to better understand their groundwater resources and meet the requirements of California's Sustainable Groundwater Management Act (SGMA, 2014), the local water agencies developed a groundwater model of the subbasin using 600 driller's logs and 50 oil and gas well logs, the latter including both lithology logs and resistivity logs (Fugro West, 2016). The model covers the subbasin, extending ~2 km outside the subbasin boundary except along the eastern edge, ranges from a depth of ~120 m in the east to ~500 m in the west and contains three layers, of variable thickness, with a cell size of 150 m × 150 m.

A description of the hydrogeology of the subbasin is given in the report by Fugro West (2016). The key features defining the layers in the groundwater model are in a geologic cross-section (modified after Fugro West, 2016), the location of which is shown in Figure 1a with the cross-section in Figure 1b. The sediments within the subbasin are divided into an upper and lower aquifer in the western half by a confining clay layer, the Corcoran Clay. The aquifers are described as Quaternary alluvium with numerous interbedded sands and clays. Generally, more clays are present in the lower aquifer than in the upper aquifer. The Corcoran Clay is described as Quaternary lacustrine and marsh deposits. The aquifers are underlain by bedrock in the east which abuts low permeability sediments to the west along a boundary interpreted to be the Rocky Hill Fault.

The groundwater model contains three layers: the upper aquifer which ranges from 100 m to 150 m in thickness; the Corcoran Clay which ranges from 10 m to 20 m in thickness, and the lower aquifer which ranges from 200 m to 350 m in thickness. Note that the three layers are defined throughout the model. In the current groundwater model the extent of the Corcoran Clay was modified from the work of Page (1986) using available well data (Fugro West, 2016) and corresponds to the location where the Clay is no longer continuous. Where the Corcoran Clay is absent, the three layers effectively become a single aquifer. As shown in Figure 1b, the base of

the model in the east is defined by the top of the bedrock, then going west is interpreted to lie at the top of the package of low permeability sediments.

Both the top of the bedrock and the location Corcoran Clay are important large-scale features of the groundwater model, the former defining the position of a no-flux boundary and the latter controlling the hydraulic connectivity between the upper and lower aquifers; thus, the accuracy of their locations and the thickness of the Clay directly impacts the accuracy of model predictions. The spatial coverage of the well logs used to constrain the depth to bedrock was poor (GKGSA, 2020), due to the fact that there were relatively few wells reaching the bedrock surface. While the spatial coverage of the well data used to map the location of the Corcoran Clay was reasonably good, there are concerns about the quality of the well data (e.g., a large locational error (~ 2 km) for the driller's logs) and interpretations of continuity between wells, particularly at the edges of the Clay where it becomes discontinuous.

2.2 The AEM method

The AEM method uses electromagnetic induction to obtain information about the resistivity of the subsurface. Time-varying electric currents are injected through a transmitter loop suspended below an aircraft to generate induced currents in the subsurface. These induced currents will depend upon the resistivity of the subsurface and generate an induced voltage that can be measured at a receiver loop also carried by the aircraft. The aircraft moves continuously while the receiver loop is recording, with the raw voltages stacked at predetermined intervals to provide measurements referred to as AEM soundings or the observed AEM data.

Inversion of the observed AEM data is necessary to obtain a 3D resistivity model of the subsurface resistivity. In hydrogeologic applications, a spatially-constrained inversion approach (Viezzoli et al., 2008) is most commonly used to recover, at each AEM sounding location, a vertical 1-D profile of resistivity fitting the observed AEM data. The spatial constraints, favoring a smooth transition of resistivity values between adjacent sounding locations, are implemented in the inversion through a regularization function. The regularization function also includes a reference model through a smallness constraint (Oldenburg & Li, 2005). Conventionally, an L_2-norm is used for the constraints in the regularization function. In this study, in addition to an L_2-norm we utilized an L_p-norm which makes it possible to incorporate additional prior knowledge (Fournier & Oldenburg, 2019).

The AEM inversion is non-unique, i.e., there are many resistivity models that can fit the data. A typical form of non-uniqueness is the presence of a depth, commonly referred to as the depth-of-investigation (DOI), below which resistivity changes in the model do not make a noticeable difference in the AEM response. We used Oldenburg and Li's (1999) approach performing two inversions with different homogeneous reference models to define the DOI. Another well-known form of non-uniqueness, of specific relevance to our study, is due to the fact that the AEM response is sensitive to the conductance of a layer, which is the thickness divided by the resistivity (Geowissenschaften et al., 2007); so neither the resistivity nor the thickness of the layer can be independently resolved. Given this limitation, other reliable information needs to be incorporated into the inversion.

3 Available Data

In 2018, ~800 km of AEM data were collected over the Kaweah Subbasin using the SkyTEM 312 system (Sorensen & Auken, 2004). Figure 1a shows the AEM soundings along the flight lines of the survey, which were located to maximize coverage in the region of the groundwater model while avoiding urban areas (Kang et al., 2020). The acquisition of the AEM data was managed by, and the data processed by, Aqua Geo Frameworks (Asch et al., 2019).

Our objective was to develop an approach that would make it possible to accurately image the bedrock surface and confining clay layer using primarily the AEM data. In addition to the AEM data, we utilized data from six wells that could be considered, with confidence, to be of high quality. This included three driller's logs in the northeastern corner of the subbasin (locations shown in Figure 1a) that had been manually inspected (Steklova, personal communication, 2020). These provided point information about the depth to bedrock. We also had access to an additional three pairs of logs, resistivity (16-inch normal) and driller's logs from the same monitoring wells, referred to as Wells A, B, C (locations shown in Figure 1a), considered by the local water agencies to be of very high quality. These pairs of logs, in the western part of the subbasin, provided information about the location of the Corcoran Clay. We took each pair of logs and, at the well location, defined the depth and thickness of the Corcoran Clay.

4 Targeted inversion approach

Our targeted inversion approach included three steps; 1) L_2-norm inversions to obtain starting resistivity models, 2) L_p-norm inversions to obtain improved resistivity models, and 3) the integration of the output from the inversions and the high-quality well data to obtain 2D maps displaying the location of the two targets – the top of the bedrock and the Corcoran Clay layer. For use in the final interpolation step we selected two resistivity models – a primary (the better) model and a secondary model, with the former interpolated to generate a 2D map of the target and the latter used, with the primary model, to provide a measure of error for the purpose of weighting in the interpolation process.

For all inversions of the AEM data, we used the regularization function, $\phi_m(m)$, which can be written as

$$\phi_m(m) = \alpha_s \int \left(w_s^{\text{cell}}(m - m_{\text{ref}})\right)^{p_s} dV + \alpha_r \int \left(w_r^{\text{cell}} \frac{dm}{dr} w_r^{\text{face}}\right)^{p_r} dV + \alpha_z \int \left(w_z^{\text{cell}} \frac{dm}{dz} w_z^{\text{face}}\right)^{p_z} dV \,, \quad (1)$$

where the first term is the smallness constraint, and the two other terms are the spatial constraints, one acting in the radial direction, denoted by r, and the other in the vertical direction, denoted by z; m and m_{ref} indicate an unknown, to be recovered, resistivity model and a reference model, respectively. The unknown and reference resistivity models were defined at each AEM sounding location with resistivity values assigned in 39 vertical cells; the thickness of a cell at the ground surface was 3 m and increased at a constant rate resulting in a total depth of 550 m. Alpha values, $\alpha_s, \alpha_r, \alpha_z$, determine the relative importance of each term. Given that layered sediments are the dominant materials in the study area, α_z was set to five times smaller

than α_r to indicate our preference for laterally-continuous rather than vertically-continuous structure; α_r was fixed to 1. The value of α_s was set to either include (α_s= 1) or not include (α_s= 0) the smallness constraint in the regularization function.

The exponent p acts on all the constraints. In terms of the smallness constraint, p influences the form of the resulting distribution of all the resistivity values in the 3D resistivity model. The conventional L_2-norm inversion, which corresponds to setting p=2, favors a smooth Gaussian distribution, where the center of the distribution is the reference model. In the L_p-norm the value of p can vary from 0 to 2 (Fournier & Oldenburg, 2019), which has the impact of favoring distributions that vary from sparse (isolated peaks) at low values of p, to Gaussian at p=2. The extreme value of p=0 denotes a distribution that has the fewest possible number of peaks deviating from the reference model.

The value of p also acts on the spatial constraints. Setting p=2 denotes a smooth transition in resistivity values in space (laterally and vertically). The extreme value of p=0 indicates a model with an abrupt transition – a large resistivity contrast, at the fewest number of interfaces between cells possible while still fitting the data. Assuming that the greatest resistivity contrast will be found at the interfaces (lateral and vertical) between hydrogeologic units, not within the units, this allows an abrupt transition only at an interface between subsurface units.

While the model space for the solution with the L_2-norm is convex, making it relatively straightforward to solve the optimization problem, when $p \leq 1$ the model space for the L_p-norm is non-convex making it challenging to find a solution. The L_p-norm has been implemented for the spatial constraints in the inversion of AEM data (often referred to as a sharp inversion) (Vignoli et al., 2015). In this study, we implemented the L_p-norm for both the spatial and smallness constraints. This had not been previously done, and introduced an even greater challenge to finding a solution given the increased level of non-convexity, but provided the enhanced flexibility we desired for incorporating prior knowledge.

The cell-based and face-based (where "face" refers to interface between the cells) weightings (w^{cell} and w^{face}, respectively) capture the level of confidence in the smallness constraint and spatial constraints at a given cell or face; the greater the weighting, the higher the level of confidence.

To conduct our inversions we used SimPEG, a Python-based open-source geophysics software package (Cockett et al., 2015; Heagy et al., 2017). Further details regarding the solution of the inverse problem can be found in Appendix A.

4.1 Step 1: L_2-norm inversions

The parameters used in all inversions in our multi-step approach are given in Table 1. In Step 1, we carried out three L_2-norm inversions. The objective in this step was to obtain a domain of interest for each target; one for the top of the bedrock, D^{bedrock}, and the other for the Corcoran Clay layer, D^{clay}. These domains defined the general regions within which we identified the presence of each target. An L_2-norm inversion favoring a smooth transition of resistivity values in the lateral directions was most appropriate for this purpose. We only used spatial constraints,

setting α_s= 0 in the first inversion (Inversion 1 in Table 1) so did not need to define a reference model. This setup (or setting a very small value of α_s) is considered standard practice for the inversion of AEM data. D^{bedrock} and D^{clay} were selected from the L_2-norm inversion by visually identifying the boundaries of the targets. We then added a buffer of a few kilometers to these boundaries to ensure that we captured the full extents of the targets within the defined domains.

Given that identifying the top of the bedrock is a relatively simple target with AEM data, we decided that the model recovered from this first L_2-norm inversion was sufficiently accurate to be used, not just to define the domain, but also as the secondary model for that target. At each location in D^{bedrock}, we assigned the top of the bedrock to the depth that divided the full depth range into two depth intervals – one above and one below, with minimal variance in the resistivity values of each depth interval.

While the first L_2-norm inversion was not sufficiently accurate for locating the Corcoran Clay, we used it to identify a depth interval that would include the Clay that was used in developing reference models for the L_p-norm inversions in the next step. Identifying the top and base of the Clay was done subjectively, by selecting the top and base of a continuous low-resistivity zone in the 3D resistivity model. Note that this "Clay-containing" depth interval was on the order of 80 m to 160 m in thickness, so much larger than was expected for the thickness of the Clay alone.

Two other L_2-norm inversions (Inversions 2 and 3 in Table 1) were used, with the smallness constraint added (α_s= 1), to calculate the DOI.

4.2 Step 2: L_p-norm inversions

The L_2-norm inversions allowed us to identify the regions where our targets were present, but there was still considerable uncertainty in the exact locations of these targets. In this next step, in order to improve our ability to locate these targets, we incorporated prior knowledge specific to each target and performed an L_p-norm inversion(s) within the domain of interest for each target.

Our prior knowledge was based on a general understanding of the hydrogeology of the study area (Faunt, 2010; GKGSA, 2020) and familiarly with the resistivity of geologic materials. In terms of locating the top of the bedrock, given the composition of the aquifers and the bedrock in the study area, we used the fact that there should be a large resistivity contrast at the interface between the bedrock and the overlying aquifer. In locating the Corcoran Clay, we used the fact that there should be a large resistivity contrast at the interfaces between the coarser-grained sediments of the aquifers and the Corcoran Clay. We also knew that the thickness of the Clay layer was generally much thinner than the over/underlying aquifers. Below we describe the methodology used to resolve each of the targets.

4.2.1 Top of the bedrock

To locate the top of the bedrock, we conducted an L_p-norm inversion (Inversion 4 in Table 2) using only the AEM data within D^{bedrock}, setting α_s=0 (only the spatial constraints were used), and the p-values of the spatial constraints (p_r, p_z) to zero. This tailored the inversion to assign a large resistivity contrast only when required to fit the data. The location of this large resistivity

contrast could then be interpreted to be the top of the bedrock and the recovered resistivity model used as the primary resistivity model for this target. In the primary resistivity model, we determined at each sounding location whether the bedrock surface was present or absent and, if present, estimated the depth to bedrock.

4.2.2 Corcoran Clay layer

Two L_p-norm inversions were conducted to locate the Corcoran Clay so as to have available a primary resistivity model and a secondary model. We defined the primary resistivity model as one that showed good agreement with the resistivity and driller's logs from Wells A and B; and the secondary resistivity model as one that showed good agreement with the resistivity and driller's logs from Well B. Both L_p-norm inversions used the same spatial constraints but a different smallness constraint by changing the reference model.

In setting the spatial constraints, we used the prior knowledge that there should be a large resistivity contrast at the boundaries of the Clay so, as was done in locating the top of the bedrock, p-values for the spatial constraints were set to zero. In addition, we incorporated the fact that the Clay is much thinner than either the overlying upper aquifer or underlying low aquifer. In a recovered resistivity model therefore, most of resistivity values should correspond to the aquifer materials and relatively few to the Clay. To obtain such a sparse distribution of resistivity values, centered on the aquifer resistivity values, we added the smallness constraint to the regularization with $p_s = 0$.

To define the two reference models used to obtain the primary and secondary models, we identified two regions: outside and inside the Clay-containing depth interval identified using the resistivity model recovered from the first L_2-norm inversion. In both reference models we set the resistivity values for the cells outside the Clay-containing layer equal to those in the L_2-norm recovered resistivity model, but varied the resistivity value of the cells inside the Clay-containing layer. We allowed the homogeneous resistivity of the Clay-containing layer, $\rho_{\mathrm{ref}}^{\mathrm{clay}}$, to range from 10 Ωm to 30 Ωm, iteratively solving for two resistivity values which, when used in the reference models, resulted in the recovery of the primary and secondary resistivity models. Given that the vertical extent of the Clay-containing layer likely included borders of the surrounding aquifers, the range of resistivity was determined by choosing 1th and 99th percentile of the resistivity values within the Clay- containing layer. Resulting values of $\rho_{\mathrm{ref}}^{\mathrm{clay}}$ for the primary and secondary models were 30 Ωm and 20 Ωm, respectively.

In the two recovered resistivity models (primary and secondary), we determined at each sounding location whether the spatially-continuous Corcoran Clay was present or absent, interpreting a large resistivity contrast at two interfaces as the top and base of the Clay. The depth to the top interface was defined as the depth to the Clay. For the Clay thickness, we could have used the distance between the top and base, but wanted improved accuracy given the inability of the AEM method to independently resolve resistivity and thickness. Representing the Clay, with total thickness T_{cc} and resistivity ρ_{cc}, as a series of layers, each of thickness T_i with resistivity ρ_i, what is captured in the AEM data is an integrated measurement that can be

represented as applying an electric field oriented parallel to these layers resulting in the following relationship:

$$\frac{\rho_{\mathrm{cc}}}{T_{\mathrm{cc}}} = \sum \frac{\rho_i}{T_i} \tag{2}$$

At an AEM sounding, the Corcoran Clay, with total layer thickness T_{AEM} and total resistivity ρ_{AEM} , was recovered in the resistivity model as a layer of two or three resistivity cells each with thickness $T_{\mathrm{c,i}}$ and resistivity $\rho_{\mathrm{c,i}}$ where

$$\frac{\rho_{\mathrm{AEM}}}{T_{\mathrm{AEM}}} = \sum \frac{\rho_{\mathrm{c},i}}{T_{\mathrm{c},i}} \tag{3}$$

We wanted to accurately recover the true T_{cc} as opposed to T_{AEM}. We accomplished this through a calibration process using well data, referring to the determined thickness of the Clay as $T_{\mathrm{calibrated}}$ and the determined resistivity of the Clay as $\rho_{\mathrm{calibration}}$.

For the primary model, we had sounding locations close to Wells A and B. From the resistivity logs from Wells A and B, we had estimates of the thickness of the Clay, $T_{\mathrm{cc}}^{\mathrm{wellA}}$ and $T_{\mathrm{cc}}^{\mathrm{wellB}}$, respectively. For an AEM sounding close to the location of Well A we could write

$$\frac{\rho_{\mathrm{calibration}}}{T_{\mathrm{cc}}^{\mathrm{wellA}}} = \sum \frac{\rho_{\mathrm{c,i}}^{A}}{T_{\mathrm{c,i}}^{A}} \tag{4}$$

where superscript A indicates the closest sounding location to Well A. Using the two soundings closest to Well A and the two closest to Well B yields:

$$\frac{\rho_{\mathrm{calibration}}}{T_{\mathrm{cc}}^{\mathrm{wellA}}} + \frac{\rho_{\mathrm{calibration}}}{T_{\mathrm{cc}}^{\mathrm{wellB}}} = \sum \left(\frac{\rho_{\mathrm{c,i}}^{A}}{T_{\mathrm{c,i}}^{A}} + \frac{\rho_{\mathrm{c,i}}^{B}}{T_{\mathrm{c,i}}^{B}} \right) \tag{5}$$

Rearranging this, we obtain

$$\rho_{\mathrm{calibration}} = \frac{\Sigma \left(\frac{\rho_{\mathrm{c,i}}^{A}}{T_{\mathrm{c,i}}^{A}} + \frac{\rho_{\mathrm{c,i}}^{B}}{T_{\mathrm{c,i}}^{B}} \right)}{\frac{1}{T_{\mathrm{cc}}^{\mathrm{wellA}}} + \frac{1}{T_{\mathrm{cc}}^{\mathrm{wellB}}}} \tag{6}$$

The calibration process, resulting in a calibrated clay thickness, $T_{\mathrm{calibrated}}$ can be written as

$$T_{\mathrm{calibrated}} = \frac{T_{\mathrm{AEM}}}{\rho_{\mathrm{AEM}}} (\rho_{\mathrm{calibration}})^{-1} \tag{7}$$

This calibration was applied to all values of Clay thickness (T_{AEM}) obtained from the primary resistivity model to obtain our best estimates of Clay thickness. The calibration resistivity of the primary model was 5 Ωm.

The same procedure was applied for the secondary model, but the Clay was only found to be present at the sounding location closest to Well B, not at the sounding location closest to Well A. Therefore, only Well B was used in the calibration, so the calibration resistivity became: $\rho_{\text{calibration}} = T_{\text{cc}}^{\text{wellB}} \sum \frac{\rho_{\text{c,i}}^{B}}{T_{\text{c,i}}^{B}}$. The resulting calibration resistivity for the secondary model was 7 Ωm.

4.3 Step 3: Integration of data to generate maps of targets

The locations of the targets were obtained from Steps 1 and 2 at each sounding location. In this step, the locations of the targets from the AEM data were integrated with the high-quality data from six wells to generate 2D maps of the targets on a uniform grid with a cell size of 150 m, which is the same as the groundwater model. The accuracy of the depth to the bedrock surface and to the Corcoran Clay that we were able to obtain from AEM data was limited by the thickness of the resistivity cells. Therefore we used the thickness of the resistivity cell at the target depth to provide a measure of error in the 2D maps. Due to the calibration process, the estimated Clay thickness was not limited by the thickness of the resistivity cell. The fact that the calibration resistivity values were 5 Ωm and 7 Ωm indicated that there could be roughly 30% relative error in the estimate of the Clay thickness.

4.3.1. Top of the bedrock

The top of the bedrock was displayed in a 2D map as the depth to bedrock. For developing this map, the input data were: (1) depth to bedrock from the three driller's logs, (2) depth to bedrock estimates at all sounding locations in the primary and secondary resistivity models within D^{bedrock} where the bedrock surface was determined to be present in Step 2.

The depth to bedrock values from the primary model, $d_{\text{target}}^{\text{aem}}$, were interpolated giving higher weighting to the values with lower errors; with error defined as the absolute difference between the estimates from the primary and secondary models. The depths extracted from the three driller's logs, d^{well}, were used as hard constraints. Given the degradation in the lateral resolution of AEM data with depth, an estimate of the depth to bedrock obtained at a sounding location was assigned to an area, the radius of which depended upon the depth, z_{target}. The definition of this radius is based upon the propagation of induced currents in a homogeneous subsurface (Nabighian, 1979), and is given by the following equation:

$$r^{\text{aem}} = z_{\text{target}}\sqrt{3} + r^{\text{tx loop}} \tag{8}$$

where $r^{\text{tx loop}}$ is the effective radius of the transmitter loop; $r^{\text{tx loop}}$ was 11 m. Assigning depth values to the 2D map was done through an averaging function, $F_{\text{avg}}[\cdot]$, which averages grid values of the 2D map, m^{2D}, within the distance r^{aem} from each sounding location:

$$d_{\text{target}}^{\text{aem}} = F_{\text{avg}}[m^{2D}; r^{\text{aem}}] \tag{9}$$

The interpolation is an inverse operation of equation 8, which can be written as

$$m^{2D}(x,y) = F_{avg}^{-1}[\, d_{target}^{aem}, \delta d_{target}^{aem}, d^{well}] \quad (10)$$

where δd_{target}^{aem} indicates the measure of error. The solution of this inverse problem adopted the framework used for the inversion of the AEM data (Appendix A). Given that this inverse problem was non-linear due to the imposed hard constraints, providing a starting 2D map of the depth to bedrock was required. For this, we used an inverse distance weighting of d_{target}^{aem} to populate all cells in the 2D grid.

To incorporate our preference that the depth to the bedrock varies smoothly in the lateral direction, we only used the spatial constraints for a regularization function, which can be written as

$$\phi_m(m) = \alpha_x \int \left(\frac{dm}{dx}\right)^2 dV + \alpha_y \int \left(\frac{dm}{dy}\right)^2 dV \quad (11)$$

Both alpha values for the spatial constraints were set to 1, providing an equal weighting in the x- and y- directions.

4.3.2. Corcoran Clay layer

The location of the Corcoran Clay was displayed in two 2D maps as the depth to the top of the Clay and the Clay thickness. As was done for mapping the depth to bedrock, we interpolated the weighted-by-error locations of the Clay layer from the primary resistivity model, using the secondary model to estimate error. We included values for the depth to the Clay only at sounding locations where the Clay was identified in the primary resistivity model from Step 2. We included values for the Clay thickness at all sounding locations within D^{clay} with the thickness given as 0 at any sounding location where the Clay was not identified. The three pairs of well data were used as hard constraints. The starting 2D map was generated by using the inverse distance weighting of the locations of the depth to the Clay and Clay thickness from the primary resistivity model.

5 Results

The DOI, obtained in Step 1 using an L_2-norm inversion, ranged from 240 m to 380 m which covers the depth range within which both of the targets are present in the groundwater model. The domains of interest for the targets, obtained in Step 1 using an L_2-norm inversion, are shown in Figure 2. As expected, $D^{bedrock}$ was located along the eastern edge of the subbasin and D^{clay} in the western half. In Figure 2 we also show the locations within the domain of interest for each target where the target was determined, from the L_p-norm inversion, to be absent; in the figure we show each tenth sounding (~200-300 m spacing). As seen in the figure, there was a large AEM data gap at the center of the survey area due to the presence of urban areas. This resulted in

a high level of uncertainty in using AEM data to map the extent of the targets in these areas. Shown in the figure are the western boundary of the bedrock, and the northern and eastern boundaries of the Clay from the groundwater model. The comparison with the results obtained from the AEM data will be discussed in a later section.

In Figures 3 and 4 we show, along two selected transects B-B' and C-C' (locations in Figure 2), vertical sections displaying the resistivity models recovered from the L_2-norm and L_p-norm inversions. All visualizations of recovered resistivity models are shown between the ground surface and the average DOI of 300 m. The section in Figure 3 focuses on the top of the bedrock, and Figure 4 on the Corcoran Clay with a larger resistivity range (5-300 Ωm) shown in Figure 3 than in Figure 4 (8-100 Ωm).

The sections in Figure 3 extend from B, at the western limit of D^{bedrock}, to B'. Included on the sections are three driller's logs which describe bedrock and the overlying sediments. In Figure 3a (L_2-norm) we interpreted the most resistive unit to be the bedrock, but found a smooth transition from the bedrock to the overlying lower resistivity materials. The top of the bedrock, obtained using the minimal variance approach, falls within the depth range corresponding to this transition. Using the L_p-norm inversion, with the recovered model shown in Figure 3b, we found an abrupt change in resistivity between the bedrock and overlying lower resistivity materials, the depth of which is in good agreement with what is seen in the driller's logs. Moving from east to west (B' to B), we see a sharp close-to-vertical interface separating resistive bedrock (to the east) from lower resistivity sediments (to the west). These lower resistivity sediments are identified, at shallower depths in the driller's log just east of this interface, as predominantly clay. This lateral location along B-B', which is referred to as B1, is marked as a vertical dashed line. All bedrock in regions westward of this location will be beneath the DOI so not seen in the AEM data. This location is interpreted as the western limit of the bedrock in this transect. This same vertical interface between bedrock and sediments was found for other flight lines within D^{bedrock} and defined as the western limit of the bedrock.

In Figure 4a is a vertical section extending from C to C' (on Figure 2) which displays the resistivity model recovered from the first L_2-norm inversion. The interpreted location of the layer that contains the Corcoran Clay corresponds to the zone of lower resistivity varying in thickness from 80 m to 160 m. In Figures 4b and 4c, which extend from C to the northern limit of D^{clay}, we show the primary and secondary resistivity models for the Clay recovered from the L_p-norm inversions. For both of these models the interpreted location of the Corcoran Clay lies within the depth range of the Clay-containing layer located using the L_2-norm inversion, but the thickness is significantly reduced. In the primary model close to the northern boundary of D^{clay}, we see a location where the continuous portion of the Clay ends, which is referred to as C1; this is defined in this section as the northern boundary of the Corcoran Clay.

In Figure 5, we compare 1D profiles from the three resistivity models shown in Figure 4 with the resistivity logs and sediment type information at Wells A and B within the depth range of 0 m to 250 m from the surface. As expected, for the recovered resistivity model from the L_2-norm inversion we see a gradual transition in resistivity values around the top and base of the Clay, leading us to (subjectively) identify a Clay-containing layer. The depth to the top of this layer is about 60-80 m and its thickness ranges from 80 m to 160 m. We note, that if only an L_2-norm

inversion were available, this Clay-containing layer would likely be interpreted as the location of the Corcoran Clay. In contrast to what is seen in the L_2-norm resistivity model, the primary resistivity model (from the L_p-norm inversion) shows a sharp transition in resistivity values across the top and base of the Clay. The interpreted location of the Clay agrees well with the driller's logs at Wells A and B, and corresponds to a depth interval where there are significant changes in the resistivity logs. The resistivity values in the model are lower than those in the logs by a factor of 1.5-2, likely to due to a bias towards sampling conductive materials in the AEM method. The secondary resistivity model shows good agreement with the logs from Well B, but fails to match the resistivity values in Well A. This was interpreted to be due to the underestimation of the reference resistivity value, $\rho_{\mathrm{ref}}^{\mathrm{clay}}$.

We now present our results as 2D maps in Figures 6 and 7. While we have results, from the interpolation process in Step 3, throughout the entire domains of interest for each target, the uncertainty will increase as the distance from an AEM sounding increases. We thus elected to display only those results that were within 3 km of an AEM sounding. We compared the 2D maps to the existing groundwater model by calculating the difference in areas where both our 2D maps and the groundwater model contain the targets.

The 2D map displaying the depth to bedrock is shown in Figure 6a. The first feature to note is the solid red line which represents the western boundary of observed bedrock in the AEM data This boundary was located by connecting the locations of the most-western soundings where bedrock was present. In some places, the location of this boundary is well-defined, constrained between two soundings that are close together; e.g., one to the east where bedrock was present and to the west where bedrock absent. In a number of locations, however, the uncertainty in the location of this western boundary is relatively high, increasing as the distance to an AEM sounding increases. There are differences between our mapped western boundary and that defined in the groundwater model that cannot be explained by this uncertainty alone and are not due to a limitation in the DOI of the AEM data. The depth to bedrock in the groundwater model ranges from 100 m to 170 m below the surface; this depth range is located above the DOI and is a depth range within which the sensitivity of the AEM data is relatively high.

The depth to bedrock determined from the AEM data generally increases towards the west resulting in a thickening of the package of sediments overlying the bedrock. The depth to bedrock, on average 60 m, ranges from 15 m $\pm$ 4 m to 160 m $\pm$ 14 m, where the error is due to the thickness of resistivity cells at these depths. In Figure 6b, we display the difference obtained when subtracting the depth to bedrock in the groundwater model from the depth that we determined. The depth that we determined was always less, with the difference averaging -80 m and ranging from -150 m to -5 m.

In Figures 7a and 7b, we present 2D maps displaying the thickness of and the depth to the Corcoran Clay, respectively. The blue solid line contours where the thickness (determined through interpolation in Step 3) is zero, which we define as the northern and eastern boundary of the continuous portion of the Clay. As was the case in mapping the extent of the bedrock, the uncertainty in the location of this boundary increases as the distance to an AEM sounding increases. We again observe differences in the lateral extent of the Clay interpreted from the AEM data and that shown in the groundwater model. The Clay thickness, as interpreted from the

AEM data, increases towards the southwest, with localized thinning or thickening. The thickness averages 17 m, ranging from 3 $\pm$ 1 m to 25 $\pm$ 7.5 m; with the relative error estimated from the calibration with the well data (~ 30% error). The depth to the Clay, averaging 100 m, also generally increases towards the southwest, ranging from 50 $\pm$ 6 m to 130 $\pm$ 12 m; with the error equal to the thickness of the resistivity cells.

In Figure 7c and 7d, we show the differences in thickness and depth – subtracting the values from the groundwater model from the values obtained with our approach. For the Clay thickness (Figure 7c) we found relatively large differences of -15 m to -10 m in the region between the boundary of the Corcoran Clay in the groundwater model and the boundary that we determined. Elsewhere the difference ranged from -6 m to 5 m with the absolute difference averaging 3 m. The differences in the depth to the Clay (Figure 7d) averaged -15 m, ranging from -30 m to -10 m; we always found the Clay at a shallower depth. The difference is greater along the eastern and western edges of the region where we identified the presence of the Clay, than it is in the center.

6 Discussion

6.1 Comparison of the L2-norm inversion and the targeted inversion approach

Let us first consider how the targeted inversion approach, when compared to using the L_2-norm inversion alone, improved our ability to image the two targets of interest – the bedrock surface and the confining clay layer. As shown in Figure 3a, the top of the bedrock appeared in the L_2-norm resistivity model as a smooth transition between the resistive bedrock and overlying low-resistivity sediments. As a result, delineating the top of the bedrock from this model was not straightforward, requiring the use of a variance-minimization algorithm. In contrast, the L_p-norm resistivity model shown in Figure 3b revealed a sharp interface at the top of the bedrock, that we were able to recover by incorporating the prior knowledge of a large resistivity contrast between the bedrock and the overlying sediments into the spatial constraints of the L_p-norm. The good agreement with the three driller's logs gave us confidence in our approach.

In addition to using the spatial constraints in the L_p-norm inversion to locate the Corcoran Clay, the smallness constraint was added so as to also incorporate the prior knowledge that the Clay is much thinner than the over/underlying aquifers. As shown in Figure 5, what we interpreted as the Clay-containing layer in the recovered resistivity model from the L_2-norm inversion was shallower and thicker than the interpreted Corcoran Clay in the driller's and resistivity logs from Wells A and B. In particular, the thickness of the Clay-containing layer was 4 to 5 times greater than the thickness of the Clay layer seen in the well data. This is to be expected given the diffusive nature of the AEM measurement and is a clear illustration of the problem of using a resistivity model recovered from an L_2-norm inversion to interpret the thickness of a confining clay layer. The Clay layer imaged in the primary model from the L_p-norm inversion is much closer in thickness to the logs from Wells A and B (Figure 5) demonstrating the value of the L_p-norm inversion for imaging the Clay layer. An important aspect of the L_p-norm inversion was utilizing high-quality well data, without which we would have not able to select the primary resistivity model.

When compared to the conventional approach of using an L_2-norm inversion, we found that the targeted inversion approach, involving a combination of L_2-norm and L_p-norm inversions,

yielded significant improvements in our ability to image the depth to bedrock and the confining clay layer in the study area. While requiring more time and input, in the form of prior knowledge, we were able to obtain more accurate information about the locations of the large-scale features.

6.2. Comparison of the results obtained from the AEM data to the existing groundwater model

The existing groundwater model from our study area was constructed using relatively dense well data. The fact that this model was not utilized in our targeted inversion approach provided us an opportunity to assess the efficacy of our approach by comparing the locations of the targets we obtained to those in the existing groundwater model.

We start by discussing the location of the bedrock surface, where we found a relatively large difference between our approach and the groundwater model. The location we determined for the boundary marking the western extent of the bedrock (within the depth range of the groundwater model and the AEM data) differed by $\pm$5 km from the boundary location in the groundwater model. In addition, the average difference between the depth estimates was about -80 m corresponding to a relative difference of roughly 130%. In contrast to the flat top of the bedrock in the groundwater model (as illustrated in Figure 2b), our mapping showed considerable topography (i.e., variation in depth), as would be expected given the erosional history of an exposed bedrock surface. Given the lack of well data providing information about the location of the bedrock surface in the groundwater model, it is very likely that neither the extent of the bedrock surface nor the depth to the bedrock are accurately captured in the groundwater model. With the AEM data, we were able to obtain accurate imaging of the bedrock surface – in those areas where AEM data are available. The limitation with the AEM data is the lack of coverage in some areas due to the spacing of the flight lines, and the presence of urban areas (where AEM data acquisition is not allowed); but the coverage is far superior to that of the well data. In comparing the two approaches to mapping the bedrock surface, we have much higher confidence in the location obtained through targeted inversion than that shown in the groundwater model.

In building the groundwater model, a greater number of wells were available in the region of the Corcoran Clay than in the region where the bedrock surface is present. It is, however, very difficult to accurately map out the Corcoran Clay using the well data given the abundance of other clay interbeds in the upper and lower aquifers. The Corcoran Clay is blue to gray or bluish green in color so is commonly referred to in driller's logs as "blue clay". Unfortunately, the color cannot conclusively identify the Corcoran Clay as many clays in the area that lack iron oxide are blue or gray. Further, even if the description in the driller's log does not say blue, the clay might be part of the Corcoran clay, as the driller may have decided that all clays in the area were blue so it was not worth repeating. Given all of this, mapping the Corcoran Clay with AEM data can provide a valuable complement to the interpretation based on the well data.

Let us first discuss what is shown as the northern and eastern boundary of the Corcoran Clay. As seen in Figure 7a, the boundary of the Clay that we located is about 3-7 km inside (to the west of) the boundary in the groundwater model, except for a small area where our boundary extends to the east of the model boundary. In Figure 8, we compare the mapping of the Corcoran Clay – as either present or absent, in the AEM data and in the well data. In the well data we used the

description " blue clay" within the depth range of 50 to 150 m in the driller's log as an indication that Corcoran Clay was present at that location. In the region where the boundary of the Clay in the model lies to the east of what we determined, there are only three wells with "blue clay" and 18 without. Along the southern stretch of this region, our mapped boundary seems to show better agreement with the well data than the groundwater model boundary does. As evidence of the challenge of using well data to locate the Corcoran Clay in the groundwater model, it is interesting to note the 13 reports of "blue clay" in wells to the east of the boundary in the model.

One likely explanation for the difference in the boundary locations, where the AEM boundary lies inside that in the groundwater model, is the challenge of using well data to differentiate the continuous Corcoran Clay from discontinuous Corcoran Clay, or from the occurrence of other clays at a similar depth. In reviewing the resistivity models recovered from the AEM data, we see clay-rich zones in the region between the two boundaries, but these zones are not continuous with the Corcoran Clay. An example of this is shown in Figure 4, where clay is present to the east of Well C1 but it is not continuous with the Corcoran Clay. It is possible that the Corcoran Clay becomes discontinuous in this region, but was mapped as part of the continuous Corcoran Clay in the groundwater model. It is also possible that these clay-rich zones are not part of the Corcoran Clay at all, but just identified as such in the groundwater model.

In the area where our determined boundary crosses over and goes to the east of the model boundary, our boundary is not well constrained by AEM soundings due to the presence of an urban area. Nor is it well constrained in this area by the appearance/absence of "blue clay" in the driller's logs.

The advantage we have in both the AEM data, is the ability to see the continuous Clay layer. As such, we tend to put greater confidence in the location of the boundary determined from the AEM data. The key limitation is the high level of uncertainty in areas with poor AEM data coverage. If the boundary location in these areas has a significant impact on the accuracy of the groundwater model, additional data should be acquired.

In regions where the Clay was identified in the AEM data and the groundwater model, we identified small to moderate differences in Clay thickness. In the groundwater model the Clay thickness ranged from 10 m to 20 m; in our 2D map it ranged from 3 $\pm$ 1 m to 25 $\pm$ 7.5 m. The relative difference was ~15%. The depth to the Clay in the groundwater model ranged from 50 $\pm$ 90 m to 160 m $\pm$ 12 m ; in our 2D map it ranged from 50 $\pm$ 6 m to 130 m $\pm$ 12 m , again resulting in a relative difference of ~15%.

6.3 Further use of the results from the targeted inversion

While the targeted inversion approach provided accurate locations of the large-scale features of interest in this study area, there is additional information at a smaller scale that can be obtained about the groundwater system from the AEM data. This requires a high-quality resistivity model over the entire study area. To obtain such a model, we implemented a structurally-constrained inversion where information about the location of large-scale features is used to constrain the inversion. Applications to date have been in the inversion of ground-based or marine-based EM data and have used the large-scale features interpreted from seismic sections available in the

same area as the EM data (Brown et al., 2012; Key, 2009). We used the locations of the bedrock surface and the Corcoran Clay obtained from our targeted inversion approach. In using the structurally-constrained inversion, we exploited the face-based weightings in the regularization function (equation 1) to place a large resistivity contrast at the known locations of the targets and the cell-based weightings to minimize the resistivity variations in the lateral and vertical directions within the bedrock and the Clay layer. Further details about the structurally-constrained inversion can be found in Appendix B.

In Figure 9a, we show a three-dimensional view of the final resistivity model covering the entire subbasin. In the west, the Corcoran Clay divides the upper and lower aquifers, thinning out towards the east, where the upper and lower aquifers merge. In the eastern part of the basin, the resistive bedrock underlies low-resistivity sediments. As expected, we see sharp resistivity contrasts delineating the targets. In addition to delineating the targets – as had been done with the targeted inversion approach, the final resistivity model recovered from the structurally-constrained inversion also provided other information which can also be used to improve the existing groundwater model.

As shown in Figure 1b, the existing groundwater model is defined with the base at the top of a package of "low-permeability sediments" throughout much of the Kaweah subbasin and at the bedrock surface along the eastern edge. When we review a vertical section through the final resistivity model in Figure 9b (along transect D-D' shown in Figure 9a) we see low-resistivity materials adjacent to the bedrock in the east (near D') that then continue to the west for ~30 km extending to the DOI. We interpret these to be clay-rich sediments equivalent to the package of "low-permeability sediments" described in the groundwater model. The top of these sediments is above the base of the groundwater model along most of the transect. This suggests that either the base of the model needs moving to shallower depths or a new layer needs to be added to the lower aquifer. As can be seen in the 3D view of the resistivity model in Figure 9a, the package of low permeability sediments is present throughout the eastern half of the subbasin. This has important implications for groundwater flow within the subbasin and for recharge coming into the valley from the mountain block.

The resistivity model recovered from the structurally-constrained inversion provides more accurate information about the resistivity values in the upper and lower aquifers. In Figure 8c, we see a clearly imaged layer in the upper aquifer, just overlying the Corcoran Clay, with resistivity values higher than those found in the lower aquifer. This is to be expected given the reports of more clay in the lower aquifer than the upper aquifer (Fugro West, 2016). However, this resistivity feature was not clearly identified in the resistivity model recovered from either the L_2-norm inversion (Figure 3a) or from the L_p-norm inversion (Figure 3b). This demonstrates the value of the structurally-constrained inversion, where knowing the large-scale structure allows for improved imaging of the smaller-scale features.

7 Conclusions

Accurate groundwater models, to support groundwater science or management, require as input information about the large-scale structure of the groundwater system. We conclude that a multi-step targeted-inversion approach provides an effective way to extract the most accurate

information from AEM data about the large-scale structure. Having defined the large-scale structure, this can then be used to improve the recovery of the small-scale resistivity structure.

By implementing an L_p-norm inversion, we were able to incorporate prior knowledge. This made it possible to refine the recovered resistivity images so as to more accurately locate the targets. In implementing an L_p-norm inversion in other areas, the needed prior knowledge should not be difficult to obtain if information is available about the types of geological material present and the expected changes in resistivity associated with the large-scale features. The presence of high-quality well data would provide an additional source of information that could be incorporated into the inversion and would definitely result in improved imaging; but we were successful in this study with data from only six wells.

The targeted inversion approach includes multiple L_2-norm and L_p-norm inversions as well as an interpolation process, so it requires more computation and time than other approaches. We conclude, however, that this can easily be justified by the benefits obtained in terms of improved imaging. In addition, running multiple inversions could readily be parallelizable, and many of the other processes in the approach (e.g., interpolation) could be automated.

In the adoption of AEM data for the development of groundwater models, the optimal approach is to first work with all existing well data and other sources of information to develop a groundwater model, and then determine where the AEM data could be most valuable in reducing uncertainty in the model. All available data, included the acquired AEM data, would then be integrated to develop a model that fits all sources of data. Such an undertaking would require a significant effort with hydrogeologists working closely with geophysicists.

In this study we elected to use the existing groundwater model solely as a means of assessing our ability to extract information about the large-scale features from the AEM data. This allowed us to address the key question: what information *can* we obtain from AEM data to support the development of a groundwater model? This study has shown the information about large-scale structure that can be obtained from AEM data. There will inevitably be uncertainty in locating large-scale features, uncertainty that – as with well data, increases as the distance from the AEM data increases.

Given the growing use of the AEM method for groundwater science and management, we hope there will be continued development of our approach for the inversion of AEM data and integration with other forms of data, so that we can maximize the benefit of all available datasets. To accelerate this, we have publicly released the numerical codes used in this study through a Python-based open-source software, SimPEG (https://www.simpeg.xyz).

Acknowledgments, Samples, and Data

Funding for this research was provided to Rosemary Knight by the Gordon and Betty Moore Foundation (grant no. GBMF6189) and the NASA Applied Sciences Water Resources Program (award no. 80NSSC19K1248). Additional funding for the acquisition of the AEM data was obtained from a Proposition 68 Sustainable Groundwater Management grant from the California Department of Water Resources to water agencies in the Kaweah subbasin. We would like to

781 thank Aqua Geo Frameworks for providing the processed AEM data, Larry Dotson from Kaweah
782 Delta Water Conservation District for providing the geophysical logs, and Klara Steklova for
783 digitizing the driller's logs. We wish to thank Derrik Williams (Montgomery and Associates) for
784 answering numerous questions about the groundwater model. We are grateful to the SimPEG
785 community for developing and publicly releasing the SimPEG-EM1D module used in this study.
786 [Note to editors and reviewers – the following will be included once the paper has been accepted
787 for publication.] The AEM data used in this study is publicly available through the Stanford
788 Digital Library: https://sdr.stanford.edu/.
789

References

Asch, T. H., Abraham, J. D., Cannia, J. C., & Gregory, S. V. (2019). *Hydrogeologic Framework of Selected Areas of the Kaweah Sub-Basin Region in Tulare and King Counties, California*. Tulare and Kings Counties.

Brown, V., Key, K., & Singh, S. (2012). Seismically regularized controlled-source electromagnetic inversion. *Geophysics*, *77*(1), E57–E65. Retrieved from http://dx.doi.org/10.1190/geo2011-0081.1

Cockett, R., Kang, S., Heagy, L. J., Pidlisecky, A., & Oldenburg, D. W. (2015). SimPEG: An open source framework for simulation and gradient based parameter estimation in geophysical applications. *Computers & Geosciences*, *85*, 142–154. https://doi.org/http://dx.doi.org/10.1016/j.cageo.2015.09.015

Faunt, C. C. (2010). *Groundwater availability of the Central Valley aquifer, California*. *California Water Crisis*.

Foged, N., Auken, E., Christiansen, A. V., & Sørensen, K. I. (2013). Test-site calibration and validation of airborne and ground-based TEM systems. *Geophysics*, *78*(2), E95–E106. https://doi.org/10.1190/geo2012-0244.1

Fournier, D., & Oldenburg, D. W. (2019). Inversion using spatially variable mixed ℓp norms. *Geophysical Journal International*, *218*(1), 268–282. https://doi.org/10.1093/gji/ggz156

Fugro West. (2016). *WATER RESOURCES INVESTIGATION UPDATE KAWEAH DELTA WATER CONSERVATION DISTRICT*. Kaweah Delta Water Conservation District. Retrieved from http://www.kdwcd.com/wp-content/uploads/2018/07/WRI-Update-Final-Report_2016_02_29.pdf

Geowissenschaften, B. für, Knödel, K., Lange, G., Voigt, H.-J., Knödel, K., & Voigt, H.-J. (2007). *Environmental Geology : Handbook of Field Methods and Case Studies*. Berlin, Heidelberg, GERMANY: Springer Berlin / Heidelberg. Retrieved from http://ebookcentral.proquest.com/lib/stanford-ebooks/detail.action?docID=338637

GKGSA. (2020). *Groundwater Sustainability Plan, Apendicies: Coordination Agreement Kaweah Subbasin*. Greater Kaweah. Retrieved from http://greaterkaweahgsa.org/resources/groundwater-sustainability-plan/

Heagy, L. J., Cockett, R., Kang, S., Rosenkjaer, G. K., & Oldenburg, D. W. (2017). A framework for simulation and inversion in electromagnetics. *Computers & Geosciences*, *107*, 1–19. https://doi.org/https://doi.org/10.1016/j.cageo.2017.06.018

Kang, S., Dewar, N., & Knight, R. (2020). The effect of power lines on time-domain airborne electromagnetic data. *GEOPHYSICS*, *86*(2), E123–E141. https://doi.org/10.1190/geo2020-0089.1

Kang, S., Knight, R., Greene, T. J., Buck, C., & Fogg, G. E. (2021). Exploring the Model Space of Airborne Electromagnetic Data to Delineate Large-Scale Structure and Heterogeneity within an Aquifer System. *Water Resources Research*. https://doi.org/10.1002/essoar.10506076.1

Key, K. (2009). 1D inversion of multicomponent, multifrequency marine CSEM data: Methodology and synthetic studies for resolving thin resistive layers. *Geophysics*, *74*(2), F9–F20. Retrieved from http://dx.doi.org/10.1190/1.3058434

Knight, R., Smith, R., Asch, T., Abraham, J., Cannia, J., Viezzoli, A., & Fogg, G. (2018). Mapping Aquifer Systems with Airborne Electromagnetics in the Central Valley of California. *Ground Water*. https://doi.org/10.1111/gwat.12656

Nabighian, M. N. (1979). Quasi-static transient response of a conducting half-space— An

approximate representation. *GEOPHYSICS*, *44*(10), 1700–1705. https://doi.org/10.1190/1.1440931

Oldenburg, D. W., & Li, Y. (1999). Estimating depth of investigation in dc resistivity and IP surveys. *Geophysics*, *64*(2), 403–416.

Oldenburg, D. W., & Li, Y. (2005). 5. Inversion for Applied Geophysics: A Tutorial. In *Near-Surface Geophysics* (Vol. 5, pp. 89–150). https://doi.org/10.1190/1.9781560801719.ch5

Page, R. W. (1986). Geology of the Fresh Ground-water Basin of the Central Valley, California, with Texture Maps and Sections. *U.S. Geological Survey Professional Paper*, *1401–C*.

Sattel, D., & Kgotlhang, L. (2004). Groundwater Exploration With Aem in the Boteti Area, Botswana. *Exploration Geophysics*, *35*(2), 147–156. https://doi.org/10.1071/EG04147

SGMA. (2014). Sustainable Groundwater Management Act (And Related Statutory Provisions from SB1168 (Pavley), AB1739 (Dickinson), and SB1319 (Pavley) as Chaptered). Retrieved from https://water.ca.gov/Programs/Groundwater-Management/SGMA-Groundwater-Management

Sorensen, K. I., & Auken, E. (2004). SkyTEM–a New High-resolution Helicopter Transient Electromagnetic System. *Exploration Geophysics*, *35*(3), 194–202. https://doi.org/10.1071/EG04194

Viezzoli, A., Christiansen, A. V., Auken, E., & Sørensen, K. (2008). Quasi-3D modeling of airborne TEM data by spatially constrained inversion. *Geophysics*, *73*(3).

Vignoli, G., Fiandaca, G., Christiansen, A. V., Kirkegaard, C., & Auken, E. (2015). Sharp spatially constrained inversion with applications to transient electromagnetic data. *Geophysical Prospecting*, *63*(1), 243–255. https://doi.org/10.1111/1365-2478.12185

Wynn, J. (2002). Evaluating groundwater in arid lands using airborne magnetic/EM methods: An example in the southwestern U.S. and northern Mexico. *The Leading Edge*, *21*(1), 62–64. https://doi.org/10.1190/1.1445851

Appendix A Inversion Methodology

To find an inversion model, m, which fit the observed AEM data and favored prior knowledge in the regularization function, $\phi_m(m)$, we used SimPEG, a Python-based open-source geophysics software package (Cockett et al., 2015; Heagy et al., 2017) to minimize the following objective function, $\phi(m)$:

$$\phi(m) = \phi_d(m) + \beta\phi_m(m) \quad \text{(A1)}$$

$$\text{subject to } \phi_d \leq \phi_d^* \;\&\; m_{\text{lower}} \leq m \leq m_{\text{upper}}$$

Here ϕ_d indicates data misfit, m is an inversion model, β is a trade-off parameter, and ϕ_d^* is a target misfit; m_{lower} and m_{upper} are the upper and lower bounds of the inversion model. The inversion iteration was started with the initial guess, m_0, and repeated until a good fit of the data was found ($\phi_d \leq \phi_d^*$). The initial β value, β_0, was estimated by a power method, then decreased with a constant factor (0.5) within the iteration to reduce the importance of the regularization term. The initial guess was determined by finding a best-fitting half-space model. The upper and lower bounds of the model were set to positive infinity and negative infinity, respectively, indicating that there were no bounds constraints used.

Use of a L_p-norm in the regularization function makes the minimization problem non-convex (equation A1), and thus it was required to have an effective strategy to solve the inverse problem. We followed Fournier and Oldenburg (2019)'s strategy, which first finds a model with the L_2-norm inversion then activates the L_p-norm inversion.

Given the large range of resistivity values in the survey area, the distribution was best represented in logarithmic form; so, the inversion model was defined as:

$$m = \log(\rho^{-1}) = \log(\sigma), \quad m \in \mathbb{R}^M \quad \text{(A2)}$$

where σ is electrical conductivity (S/m) and M is the number of the inversion model, m. The data misfit function was defined as

$$\phi_d(m) = \sum_{i=1}^{N} \left(\frac{F_i[m] - d_i^{obs}}{\epsilon_i} \right)^2, \quad \text{(A3)}$$

where $F[\cdot]$ is a forward modelling operator predicting AEM data for a given model, $d^{obs} \in R^N$ is the observed AEM data; N is the number of data. The standard deviation (or data error) of the i-th datum, ϵ_i, is defined as

$$\epsilon_i = \text{relative error (\%)} \times 0.01 \times \left| d_i^{obs} \right| + \text{floor} \quad \text{(A4)}$$

The relative error and floor were set to 3% and 10^{-15} V/A-m^4 for most of sounding locations except for the locations close to the eastern edge of the survey area. We found that the signal-to-noise (S/N) ratio at the eastern edge was relatively low due to shallower bedrock surface compared to other regions. To take into account this, we assigned the greater level of data error:

10% and 10^{-14} V/A-m^4. The target misfit, ϕ_d^*, was set to N assuming the chi-squared distribution of the data error (Oldenburg & Li, 2005).

Appendix B Structurally-Constrained Inversion

After the locations of the targets were obtained from the targeted inversion approach, we applied the structurally-constrained inversion to recover the final resistivity model accurately imaging both the large-scale and small-scale structures. For this inversion, additional parameters needed to be added to the regularization function: faced-based and cell-based weightings (equation 1). For each face of the resistivity model (where "face" refers to interface between the cells), a different value of the face-based weighting (e.g., w_z^{face}) can be set; similarly, for each cell of the resistivity model a different value of the cell-based weighting (e.g., w_s^{cell}) can be set. Higher weightings indicate a higher level of confidence in the corresponding constraints. For instance, assigning larger values for the face-based weightings would make smoother transition of resistivity in lateral and vertical directions. To allow for sharp resistivity contrast at the targets, therefore, the level of confidence was decreased for the spatial constraints at the faces. For this we first found the closest faces for each target and then assigned zero for the corresponding face-based weightings while the face-based weightings for other faces were set to 1.

We used the cell-based weightings to promote smoother resistivity variations for cells corresponding to either the bedrock or the Clay compared to the other cells. Similarly, assigning larger cell-based weightings for the spatial constraints would make a smoother transition of resistivity. For cells below the top of the bedrock and within the Clay layer, we assigned a large value (10) for the cell-based weightings corresponding to the spatial constraints (i.e., w_r^{cell} and w_z^{cell}) while for other cells the cell-based weightings were set to 1.

Due to the large sensitivity of AEM data to conductive materials, it was easier for the inversion to update resistivity values around the Clay layer, which altered the boundaries of the Clay layer that we incorporated through the face-based weightings. Thus, it was necessary to provide additional constraint related to the resistivity information about the Clay to preserve the boundaries from our targeted inversion approach. For this, we utilized the smallness constraint in the regularization function (equation 1); this includes a reference model and a cell-based weighting. We generated a reference model composed of two regions: the Clay layer and others. Due to the fixed vertical thickness of resistivity cells, it was not possible to directly use the depth to the Clay and Clay thickness obtained from our approach. The top and base of the Clay were set to the closest faces resulting in small errors (~2-5 m). Due to these errors, it was necessary to apply the same calibration idea (used in Step 2) when assigning resistivity values to cells corresponding to the Clay layer. From the conductance of the Clay layer obtained from the primary resistivity model (Step 2), we calculated an equivalent resistivity value providing the same thickness of the Clay at each sounding location. For other cells, we assigned a mean resistivity value, 16 Ωm, of the recovered resistivity model from the L_2-norm inversion (Inversion 1 in Table 2). The cell-based weighting for the smallness constraint was set to 1 for cells corresponding to the Clay layer while a much smaller value (10^{-3}) was assigned for the other cells to minimize the impact of the reference model at those cells.

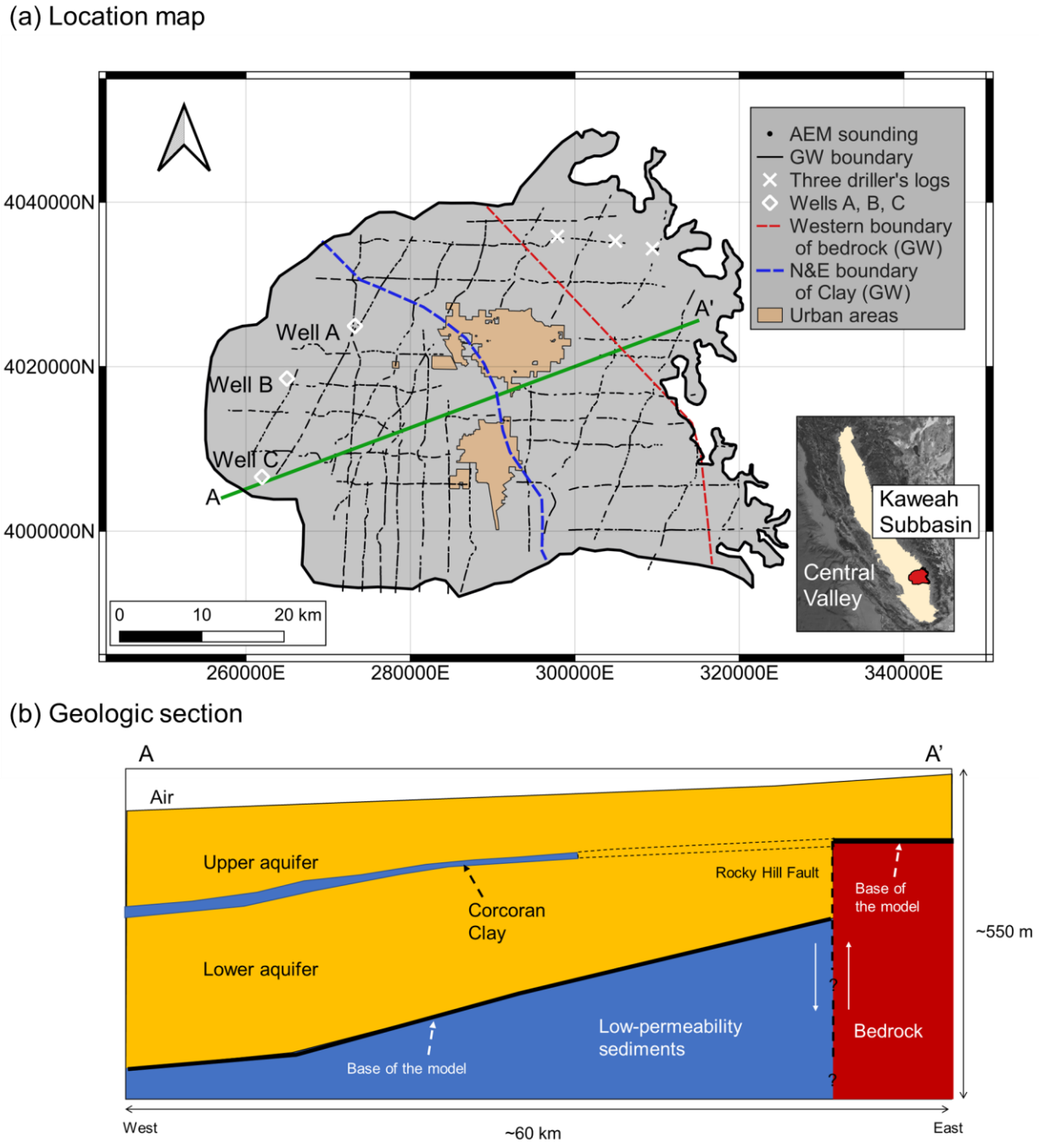

Figure 1. (a) Location map of the study area and datasets used, in the Kaweah subbasin, Central Valley of California, U.S.A. In the legend GW stands for the groundwater model. (b) Geologic cross-section located at A-A' modified from Fugro West (2016).

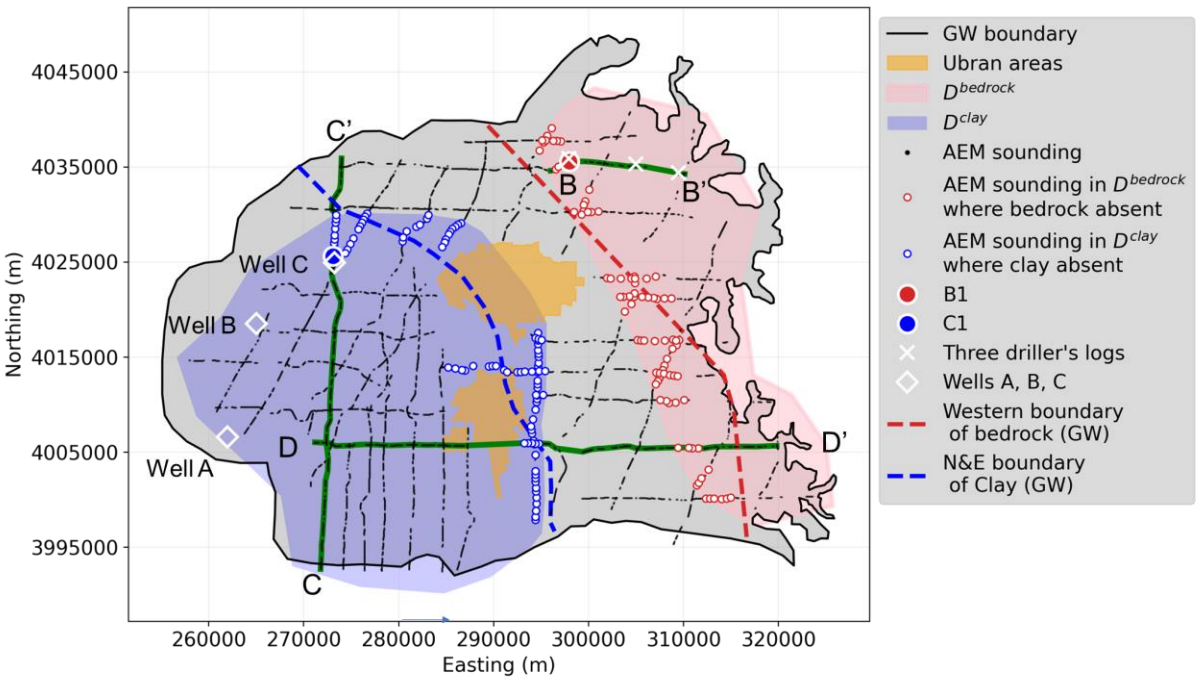

Figure 2. The extent of the groundwater model (GW) and the domains of interest for both the bedrock (D^{bedrock}) and the Corcoran Clay (D^{clay}), and sounding locations where the targets were absent within the corresponding domain of interest. For plotting these sounding locations, every 10th sounding location is shown. Also shown are the western boundary of the bedrock from the groundwater model and the northern (N) and eastern (E) boundary of the clay from the groundwater model. AEM soundings cover much of the area defined by the groundwater model with gaps corresponding to urban areas. Resistivity model(s) at transects B-B', C-C', and D-D' are shown in Figures 3, 4, and 9b, respectively.

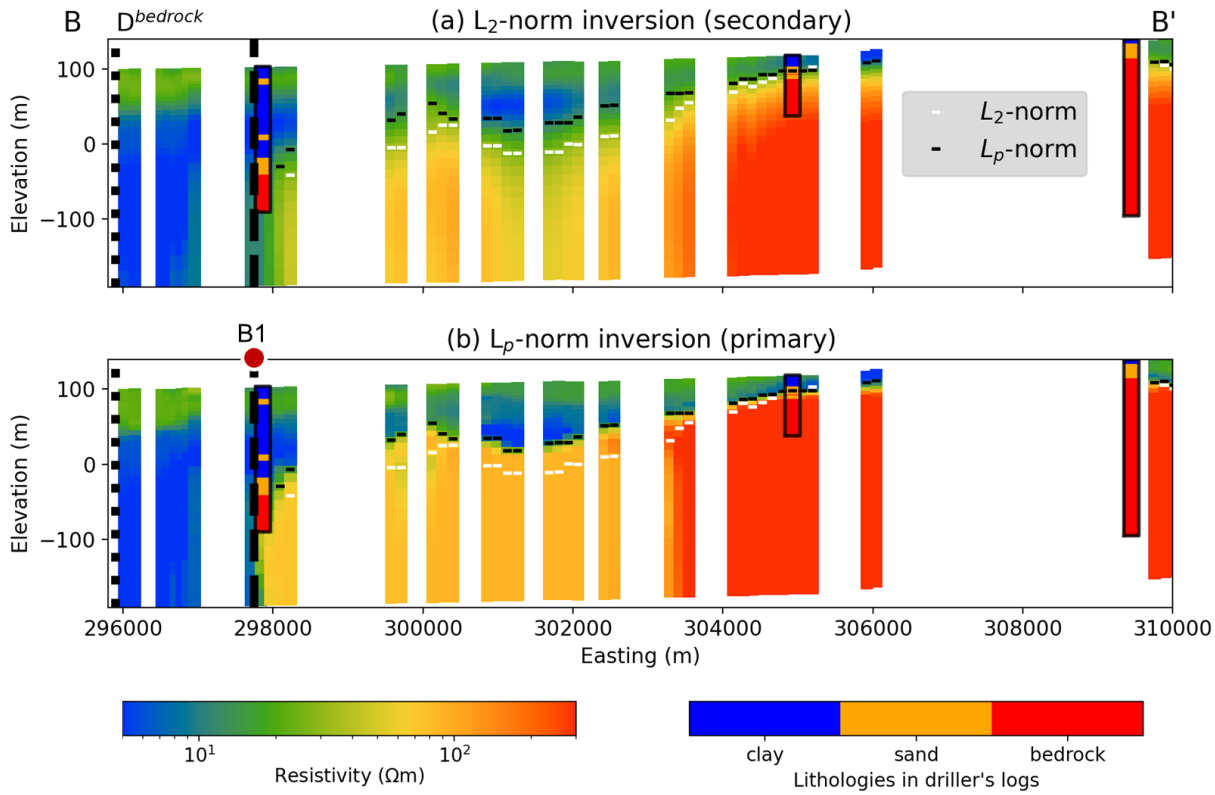

Figure 3. Comparison of the interpreted top of the bedrock in resistivity models recovered from (a) an L_2-norm inversion (secondary resistivity model) and (b) an L_p-norm inversion (primary resistivity model). Both resistivity models are along B-B' shown in Figure 2. Vertical dotted line indicates the western limit of D^{bedrock} and the dashed line indicates the location of B1 (marked in Figure 2). White gaps indicate locations where AEM data were not acquired.

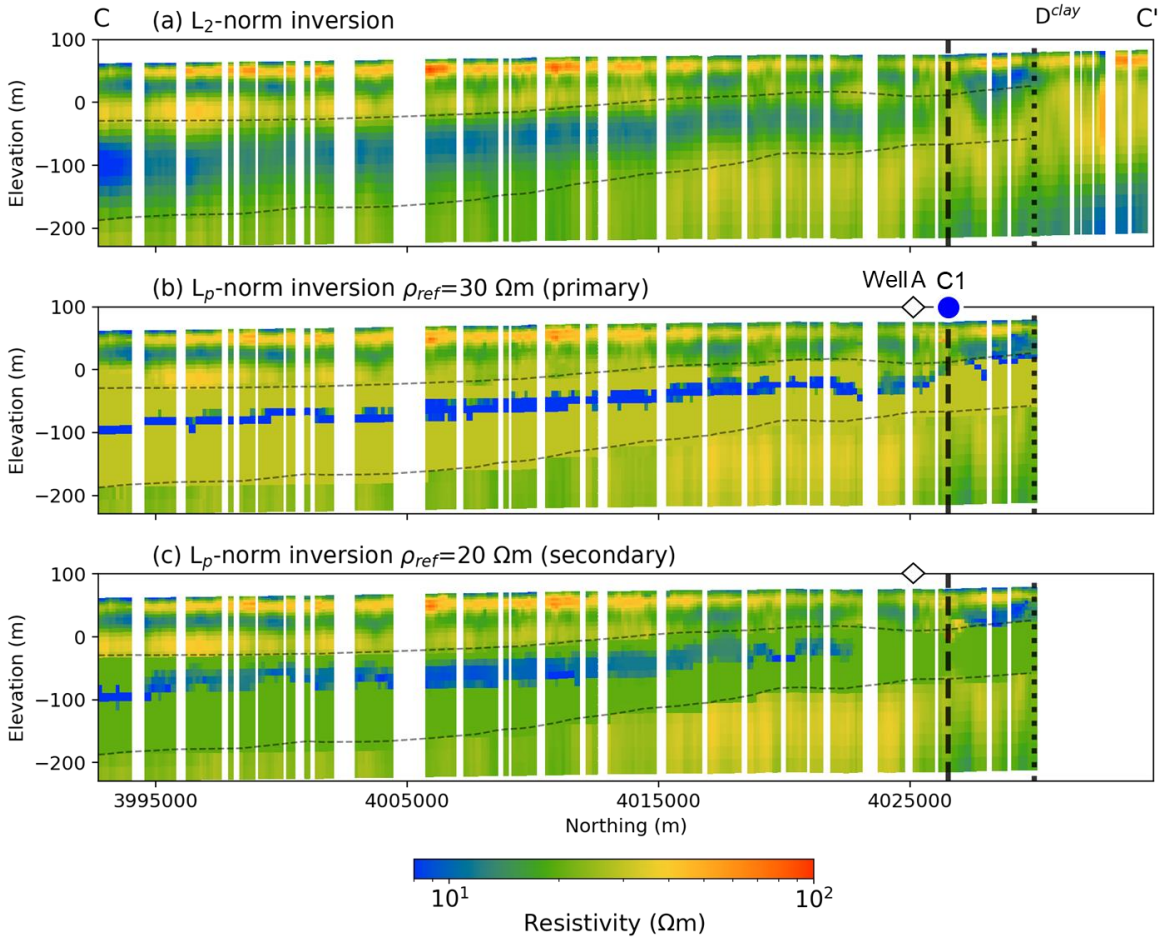

Figure 4. Comparison of the interpreted location of the Corcoran Clay in resistivity models recovered from (a) an L_2-norm inversion, (b) an L_p-norm inversion with ρ_{ref}^{clay} = 30 Ωm (primary resistivity model), and (c) an L_p-norm inversion with ρ_{ref}^{clay} = 20 Ωm (secondary resistivity model). Resistivity models are shown along C-C' in Figure 2. Horizontal black dashed lines indicate the top and base of the Clay-containing layer interpreted from the L_2-norm inversion; a vertical dashed line indicates the northern limit of the Clay. Vertical dotted line indicates D^{clay} and dashed line indicates a lateral location C1 (marked in Figure 2). White gaps indicate locations where AEM data were not acquired.

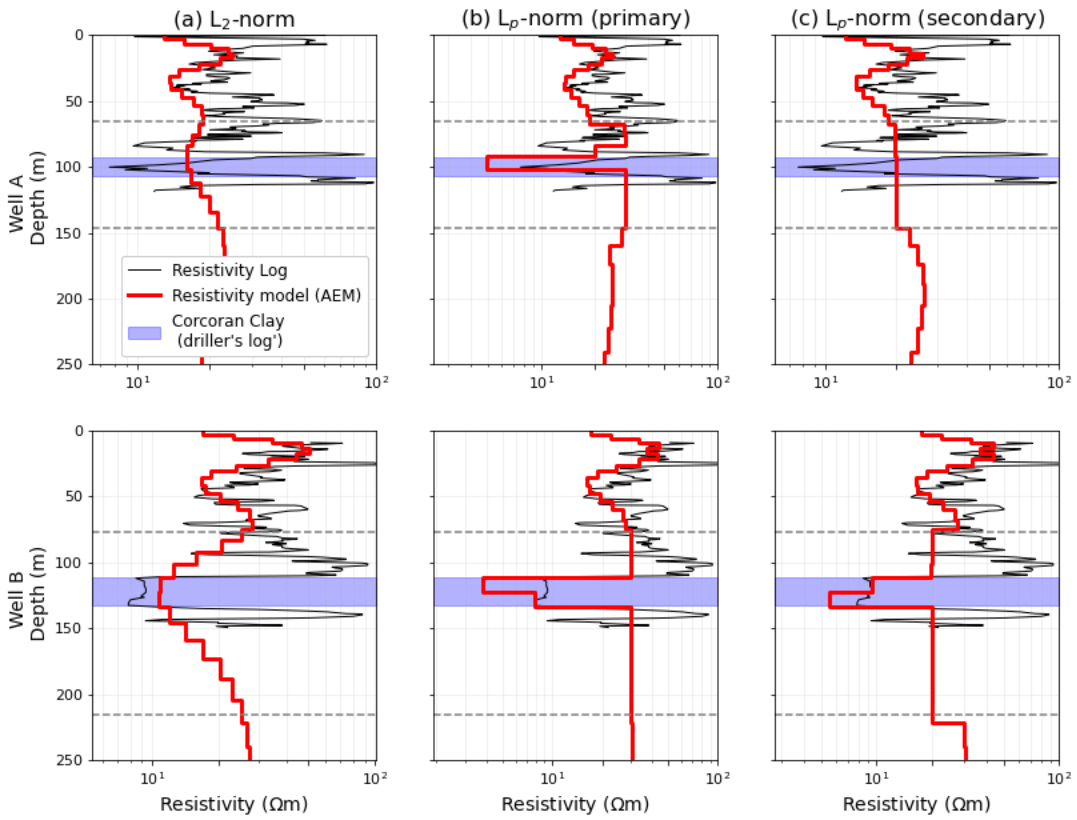

Figure 5. Comparison of the resistivity models recovered from the AEM inversions to the resistivity logs and sediment type information from Wells A and B. (a) L_2-norm inversion. (b) L_p-norm inversion with ρ_{ref}=30 Ωm (primary resistivity model). (c) L_p-norm inversion with ρ_{ref}=20 Ωm (secondary resistivity model). A blue transparent box indicates the Corcoran Clay layer identified in the driller's logs from Wells A and B. Grey dashed lines indicate the top and base of the Clay-containing layer interpreted from the recovered resistivity model of the L_2-norm inversion.

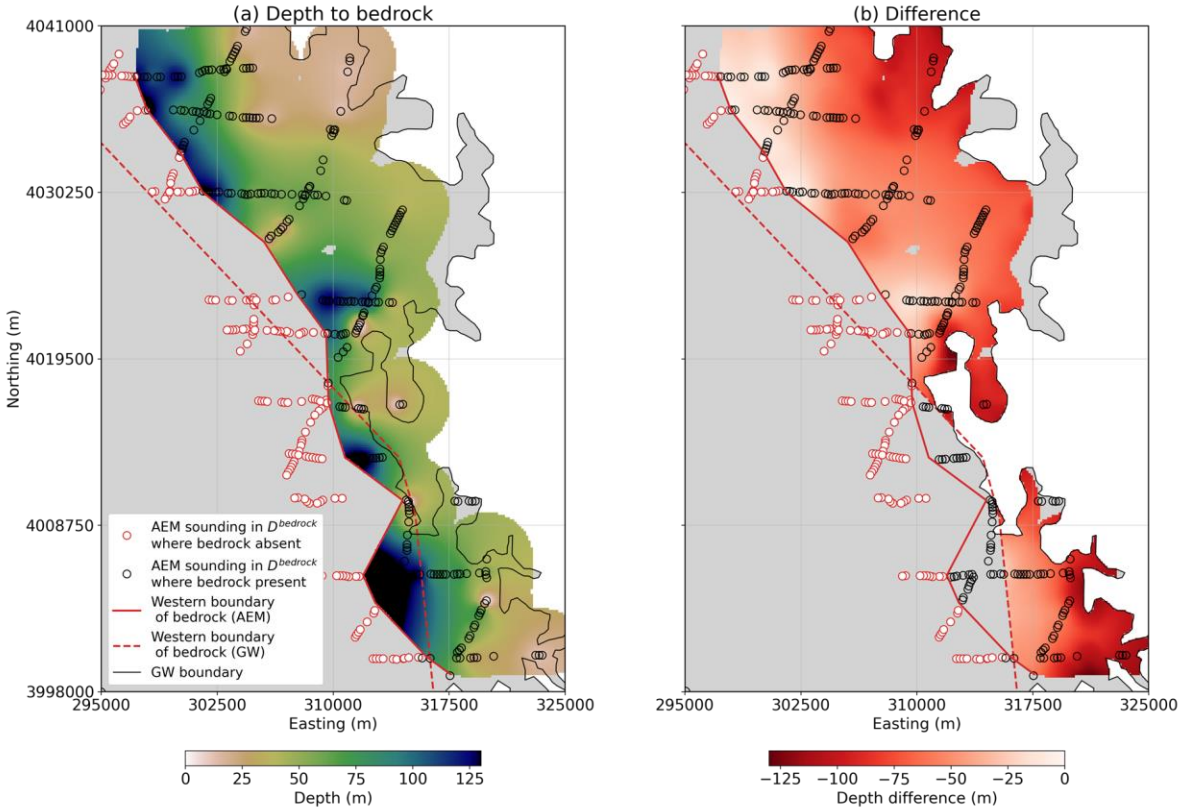

Figure 6. Two-dimensional maps showing a) the depth to the bedrock from the targeted inversion approach and b) the difference between results in a) and the depth to bedrock in the groundwater model (GW). In displaying locations where bedrock is absent or present every 10th sounding location (200-300 m spacing) is shown. Regions outside the GW are white in color.

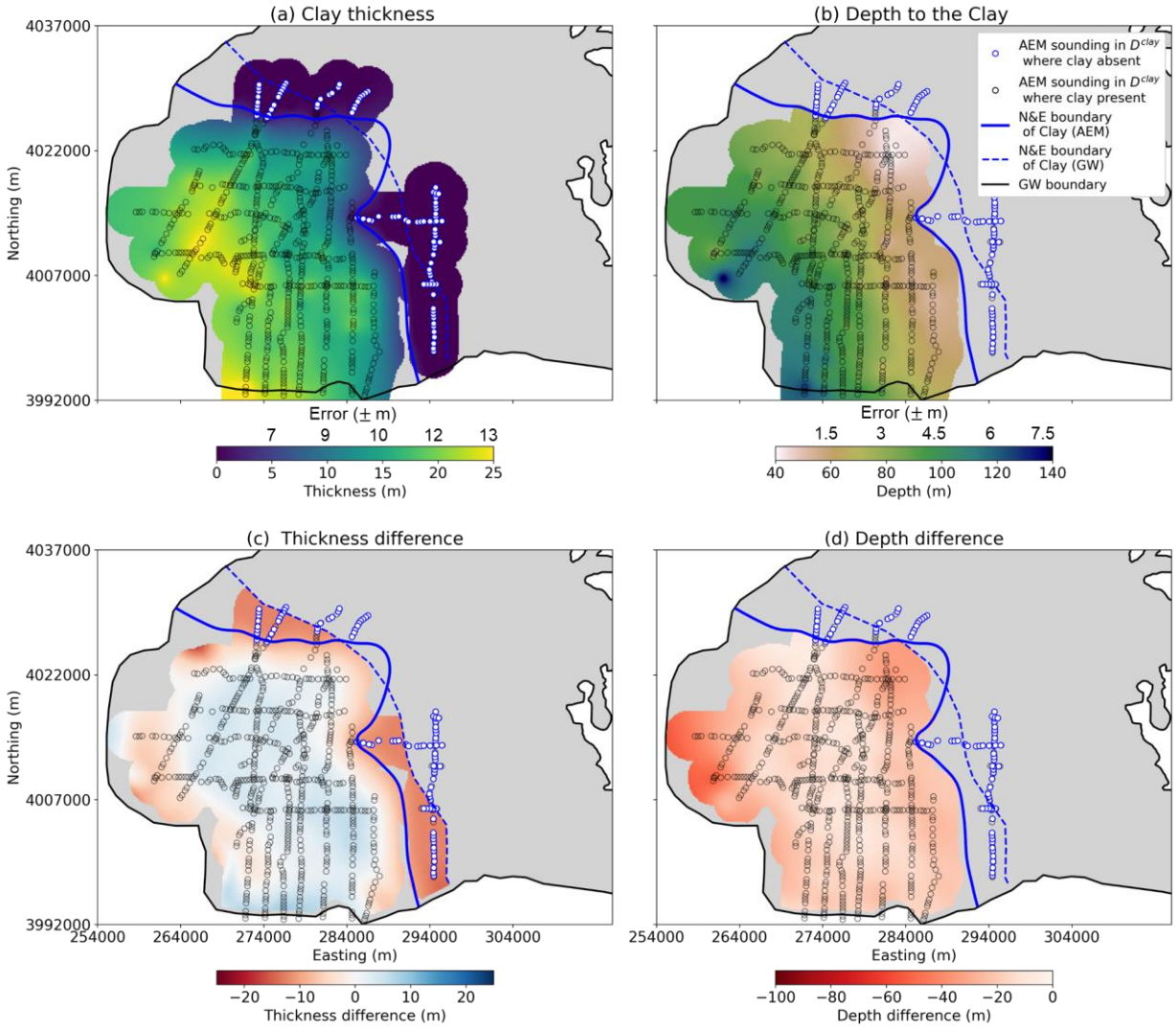

Figure 7. Two-dimensional maps showing a) the depth to the Corcoran Clay and b) Clay thickness from the targeted inversion approach. The difference between results in a) and b) and the depth and thickness in the groundwater model (GW) are shown in (c) and (d), respectively. In displaying locations where the Clay is absent or present, every 10th sounding location (~200-300 m spacing) is shown. Regions outside the GW boundary are white in color.

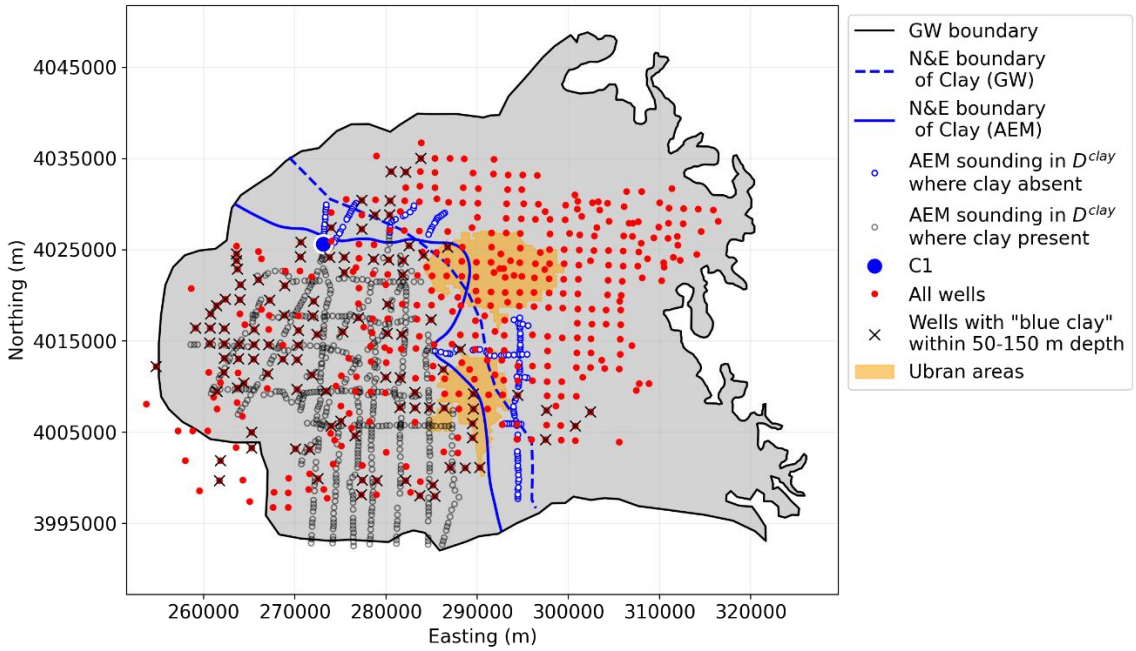

Figure 8. Location of wells used to generate the existing groundwater model, indicating those where “blue clay” was identified in the depth interval 50 to 150 m (black crosses).

(a) 3-D view of the final resistivity model

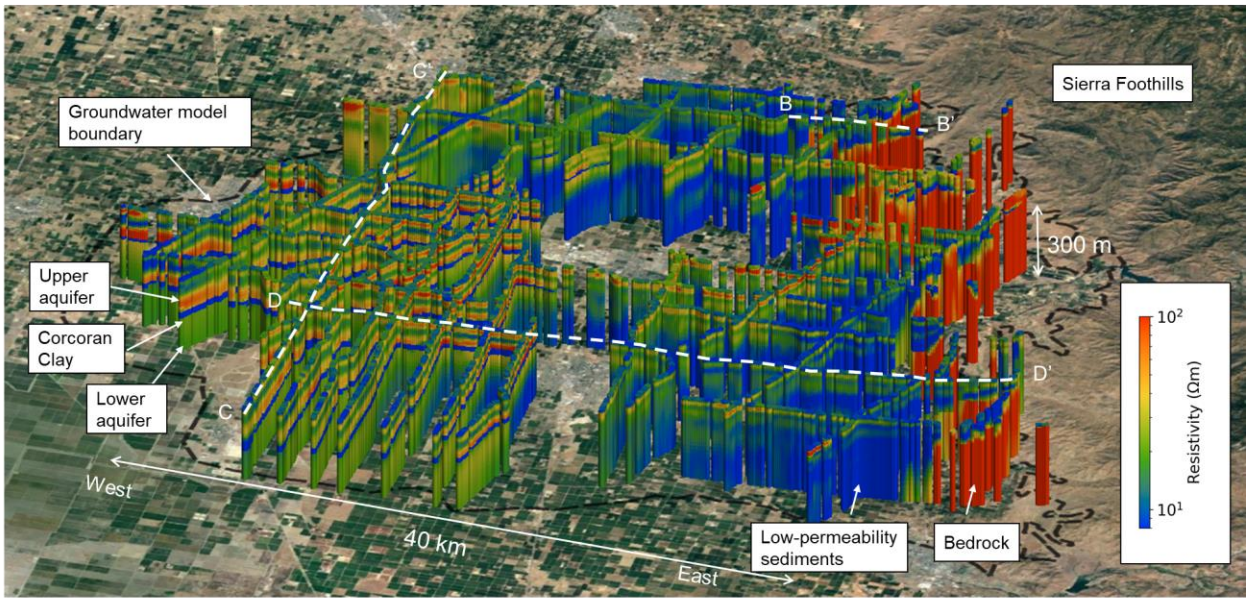

(b) The final resistivity model at a cross section: D-D'

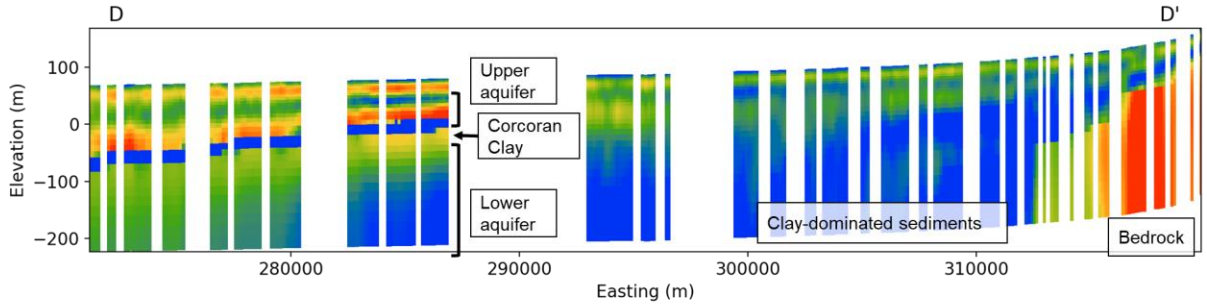

(c) The final resistivity model at a cross section: C-C'

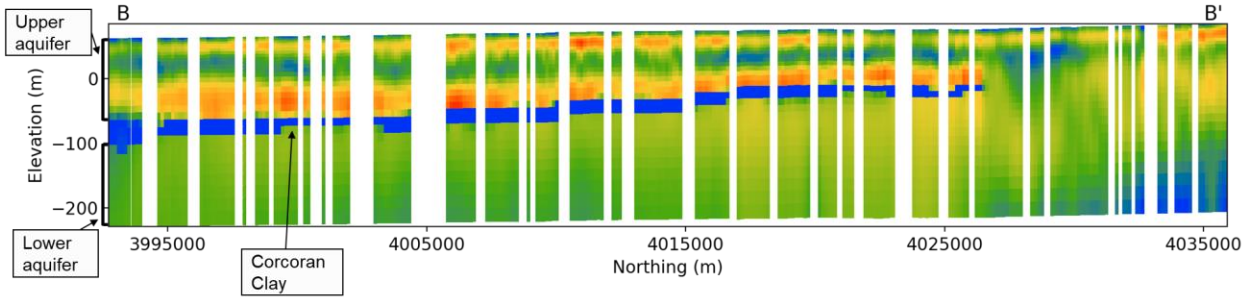

Figure 9. (a) A three-dimensional view of the final resistivity model from the targeted inversion approach. A cross-section view of the final resistivity model at vertical sections: (b) D-D' and (c) C-C'; lateral locations of the sections are shown in Figure 1a. The white gaps indicate locations where the AEM data were not collected due to our design of the AEM survey to maximize coverage while avoiding urban areas.

Table 1. Seven sets of inversion parameters used for the targeted inversion approach and the structurally-constrained inversion; the parameters are defined in equation 1. Superscripts: 30 and 20 for reference models indicate a homogeneous resistivity value, $\rho_{\mathrm{ref}}^{\mathrm{clay}}$, described in Section 4.2.2.

Inversion number	(p_s, p_r, p_z)	m_{ref}	$(\alpha_s, \alpha_r, \alpha_z)$	Inversion domain	Note
1	(N/A, 2, 2)	N/A	(0, 1, 1/5)	All soundings	Step 1: L_2-norm inversion
2	(2, 2, 2)	17 Ωm	(1, 1, 1/5)		
3	(2, 2, 2)	25 Ωm	(1, 1, 1/5)		
4	(N/A, 2, 2)	N/A	(0, 1, 1/5)	D_{bedrock}	Step 2: L_p-norm inversion
5	(0, 0, 0)	m_{ref}^{30}	(1, 1, 1/5)	D_{clay}	
6	(0, 0, 0)	m_{ref}^{20}	(1, 1, 1/5)	D_{clay}	
7	(2, 2, 2)	$m_{\mathrm{ref}}^{\mathrm{final}}$	(1, 1, 1/5)	All soundings	Structurally-constrained inversion